Experimental Techniques
https://doi.org/10.1007/s40799-023-00664-y

RESEARCH PAPER

Nine Point Bending Test Technique for Understanding of Sintered Silver Die Bonding Failure Mechanism

K. Wakamoto[1,2] · K. Fuji[1] · T. Otsuka[1] · K. Nakahara[1] · T. Namazu[2]

Received: 24 October 2022 / Accepted: 18 June 2023
© The Author(s) 2023

Abstract

The Sintered silver (s–Ag) die degradation is commonly evaluated by thermal shocked test (TST), which evaluates the material's durability against a heating/cooling cycle. Materials with different coefficient of thermal expansion (CTE) give rise to thermal out-of-plane deformation surrounding the bonding part, which deteriorates s–Ag die part by repeated thermal and mechanical stress during TST. For the safe and reliable design of s–Ag die toward long-term durability, the contribution of thermal and mechanical stresses to degradation should be understood separately. Clarify the overall s–Ag die degradation mechanism during TST compared to the new mechanical bending test that can apply out-of-plane deformation. The authors propose a new mechanical bending test technique, called the nine-point bending (NBT) test, which can provide out-of-plane deformation with a s–Ag die-attached specimen as TST like. By comparing NBT and TST, the degradation mechanism of the s–Ag die-attach element can be understood from both thermal and mechanical aspects. In scanning acoustic tomography (SAT) analysis, a similar degradation ratio between NBT and TST is obtained, which indicates that mechanical stress plays a significant role in deteriorating s–Ag die layer in TST. After 1000 cycles, however, cracking and s–Ag material aging coexist in TST only, destabilizing s–Ag die fracture. s–Ag main degradation cause in TST is clarified with mechanical stress by comparing NBT. In addition, thermally material aging destabilized the s–Ag degradation during TST.

Keywords Sintered silver · Failure physics · Die-attach reliability · Mechanical bending test

Introduction

Currently, reducing CO_2 emissions has become essential for achieving safe ecology globally. In particular, the automobile industry has taken steps toward replacing fuel vehicles with electric vehicles (EVs). In an EV, the electric power from the battery is supplied to a three-phase motor by switching the timing control of semiconductor devices. EVs are required with power control systems having high power density to minimize the vehicle body and expand their living spaces. Silicon (Si) devices are commonly adopted as switching devices. However, their performance is reaching a limitation [1]. Wide-bandgap (WBG) semiconductor materials, such as silicon carbide (SiC) and gallium nitride, have attracted much research attention because of their high electronic field breakdown and fast saturation electronic mobility. In addition, WBG devices can obtain low power loss under high-speed switching [1–3] and can operate at high temperatures exceeding 300℃ [4]. Nevertheless, a breakthrough die-attach technique is strongly demanded to extract the WBG device properties fully.

In recent years, sintered silver (s–Ag) technique has garnered much attention [5–10]. It originates from the reduction of high surface energy with nano-sized Ag particles, which can perform sintering at low-temperature bonding from 200℃ [7, 11]. After the bonding process, the s–Ag material acquires high heat conductivity of over 200 W(m/K) and a high melting point of 961℃; these values are greater than the values of a solder as a conventional die-attach material. For example, Pb–5Sn has a heat conductivity of 60 W(m/K) and a melting point of 300℃ [12, 13]. In addition, s–Ag has good tensile mechanical characteristics [14–19]. It also has a low porosity of approximately 5%, which suggested a tensile proof stress of roughly 60 MPa at 150℃; this value was about ten times higher than the Pb–5Sn value [17, 20].

✉ K. Wakamoto
keisuke.wakamoto@dsn.rohm.co.jp

[1] Power Device R&D Department, ROHM Co., Ltd., Kyoto 615-8585, Japan

[2] Faculty of Engineering, Kyoto University of Advanced Science, Uzumasa, Kyoto 615-8577, Japan

Published online: 19 July 2023

With respect to the practical use of products, s–Ag die layer degradation is commonly assessed using a thermal shock test (TST), which evaluates its material durability against heating and cooling between low and high temperatures. During TST, the s–Ag die layer experiences thermal and mechanical stresses because materials with different coefficients of thermal expansion (CTE) cause thermal warpage around a bonded part [21]. When SiC device and copper (Cu) substrate are bonded with s–Ag die layer, the s–Ag die layer starts to shrink with increasing the number of cycles. The lifetime of s–Ag die layer is defined as a delamination percentage of 20% after 1000 cycles in TST. The delamination speed is positively correlated with an accumulated plastic von Mises strain (APS) at the s–Ag die layer [22–27]. APS is calculated by modeling the target die attached assembles (DAAs) using finite element analysis (FEA), considering experimental conditions. APS can describe the plastic flowability in the die layer, which indicates that the degradation of the s–Ag die layer during TST is mainly attributed to plastic flowability. It should be noted that plastic flowability includes both mechanical stress and thermal stress components. Thus, the main contributors to the s–Ag degradation cannot be determined using only APS calculation evaluations.

Mechanical fatigue bending tests have been attempted to examine the contribution of mechanical stress on the s–Ag die layer degradation [28]. Mechanical bending test merits can precisely control the test mode using bending test speed, temperature, and frequency. However, the DAAs deformation in the conventional set-up was restricted to only one longitudinal direction due to the difficulty of the experiment technique, which could not reflect on concentric out-of-plane deformation in TST.

In this study, we developed a new mechanical bending test called nine-point bending test (NBT) that can mechanically apply similar concentric out-of-plane deformation to DAAs as TST originating from CTE mismatches during temperature variation. A comparison between NBT and TST will clarify the s–Ag degradation mechanism originating from only mechanical stress or a combination of mechanical and thermal stress. Notably, the investigation into s–Ag die layer degradation should also consider both delamination ratio evaluation by scanning acoustic tomography (SAT) observations and failure mode evaluation by cross-sectional scanning electron microscopy (SEM) observations.

Experimental Methodology

Deformation Simulation

First, FEA was performed using ANSYS 19.0 commercial software. The simulation aimed to verify the similarity of out-of-plane deformation with substrate between TST and NBT and checked the similarity of APS distribution in the s–Ag die layer between TST and NBT.

Figure 1(a) depicts the geometry, boundary condition, and mesh configuration in FEA. A one-quarter model was adopted in both TST and NBT simulations. As depicted in the left side of the model view in Fig. 1 (a), symmetric boundary conditions were applied at the side surface of each model. The TST model geometry employed SiC, s–Ag, and Cu. As shown in the top left of Fig. 1 (a), 2.4 mm square with 0.35 mm thick parts in SiC is placed onto the 10 mm square with 2 mm thick parts in Cu via the 2.4 mm square with 0.05 mm thick parts in s–Ag. The NBT model geometry employed SiC, s–Ag, Ti-6Al-4 V (64Ti), and cemented carbide. As shown in the bottom left image of Fig. 1 (a), the configuration and size of DAAs made from SiC, s–Ag, and 64Ti are identical to those in TST, except for the 1 mm thickness of the 64Ti part. In addition, two half-hemisphere and one hemisphere in 2 mm radius parts of cemented carbide are bonded at the 64Ti substrate surface as support jigs at a 45° in-plane interval with the 7 mm distance from the bottom left point position in 64Ti surface. One-half-hemisphere in a 2 mm radius block in cemented carbide parts is also bonded at the backside surface of the 64Ti parts at the bottom left corner as a loading jig. In the TST simulation boundary condition, a cyclic temperature between – 40℃ and 150℃ was set to the ambient atmosphere as a driving force. In the NBT simulation boundary condition, a cyclic force between 0 and 300 N was set on the bottom face of the jig as a driving force. Notably, s–Ag deforms plastically under applied stress at elevated temperatures [17]. Therefore, in NBT, the simulation temperature was set at 150℃ for inducing APS in the s–Ag die layer using applied mechanical force. In both TST and NBT, the stress-free temperature was set to 120℃, which was determined based on the literature [21]. Table 1 lists the input material properties for FEA, considering the elastic–plastic behavior of s–Ag as reported in the previous literature [27]. Our simulation model employed a hexagonal-type mesh element, where the elements were fixed with each other as shown in previous literature to stabilize the calculation [28]. In addition, fine mesh sizes are created at corner parts and jigs contact parts to calculate the singularity parts precisely. The model contained 9,850 meshes and 24,859 meshes for TST and NBT, respectively.

Figure 1(b) shows an out-of-plane deformation of DAAs obtained by FEA. In the TST condition, the out-of-plane deformation with a concentric concave morphology was exhibited at – 40℃; this deformation deviated by – 160℃ from the stress-free temperature of 120℃. The difference in CTE values between SiC and Cu provides thermal–mechanical stresses to the s–Ag die element, resulting in warpage deformation of the assembled model. At 150℃, the model

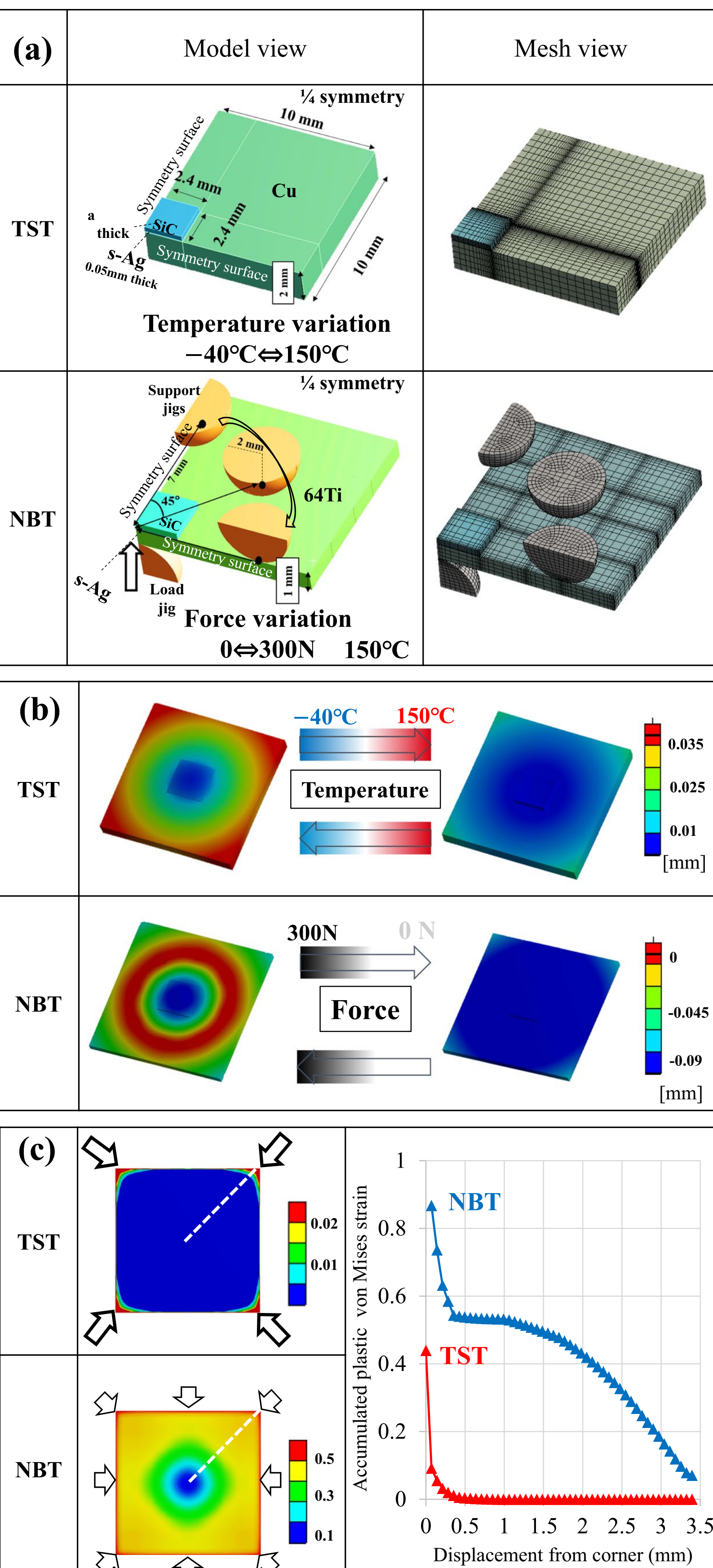

Fig. 1 (**a**) Geometry, boundary condition, and mesh configuration as used in this FEA. (**b**) Out-of-plane deformation distribution results in TST and NBT **c** Accumulated plastic von Mises strain (APS) distribution in the s–Ag layers with TST and NBT, and the changes in the APS as a function of the distance from the s–Ag die layer corner to the center

Table 1 Material mechanical properties used in FEA

Material	Young's Modulus (GPa)	Poison's Ratio	CTE ($\times 10^{-6}$)
SiC	412	0.17	3.0
Copper	118	0.35	16.8
64 Ti	115	0.35	-
s-Ag	s-Ag (RT) s-Ag (100°C) s-Ag (150°C) Stress (MPa) Strain (%)	0.35	19.5
Cemented carbide	630	0.21	-

showed an almost flat shape due to a small temperature gap from 120℃. Thermal–mechanical stresses can be cyclically applied to the bonded section through the alternative repetition of heating and cooling. Similar to the TST model, the NBT condition also exhibited a concentric concave out-of-plane deformation, albeit with different deformation profiles. This deformation disappeared after the applied force was released. Cyclic mechanical stress can be applied by repeating the force application. Both NBT and TST showed similar deformation morphologies. This result suggests that NBT can mechanically apply out-of-plane deformation to the DAA, like the TST.

The APS distribution in the s–Ag die layers with TST and NBT, and the changes in the APS as a function of the distance from the s–Ag die layer corner to the center were checked (Fig. 1(c)). In the figure, the blue color plots and red color plots indicate the APS values of NBT and TST, respectively. In the TST condition, the APS concentrated at the corner of the s–Ag layer, and its value rapidly decayed according to the inside part. In the NBT condition, the APS concentrated in the edge part and gradually decayed with a concentric profile. The highest value of the APS in NBT was approximately two times higher than that in the TST. In other words, the proposed NBT condition can lead to s–Ag die fracture with respect to possessing sufficient APS compared to that in the TST.

Experiment System

Figure 2(a) shows photographs of the NBT experiment system. As shown in the figure, the universal test system (Instron Japan: 68TM-5, Kanagawa, Japan) comprised a temperature variation chamber, a load cell, a brushless AC servomotor, a flow heater, a displacement sensor, and our designed load and support jigs. The load jig motion was controlled by external commercial software, Instron Blue Hill Universal, which also controlled the applied stress. A round-shaped cemented carbide pin was embedded at the center of the loading jig made of stainless steel alloy. The position of the load pin was fixed using a screw embedded on the lateral surface of the base jig. For the support jig, eight pins identical to the load pin were arranged in a regular octagonal position in-plane to maintain a 7-mm distance from the center of the support jig, which was also made of stainless steel alloy. A 20-mm square hole metal guide plate made of aluminum alloy was placed at the center of the base jig to guide the specimen position.

Figure 2(b) illustrates the cross-section sketch view of the NBT system. As shown in the figure, a stainless-steel spring was placed under the bottom surface of each support pin to make a uniform contact between each support pin and the substrate surface. The height of each pin was lifted to the contact position using the spring's reaction force and then fixed by fastening the side screw.

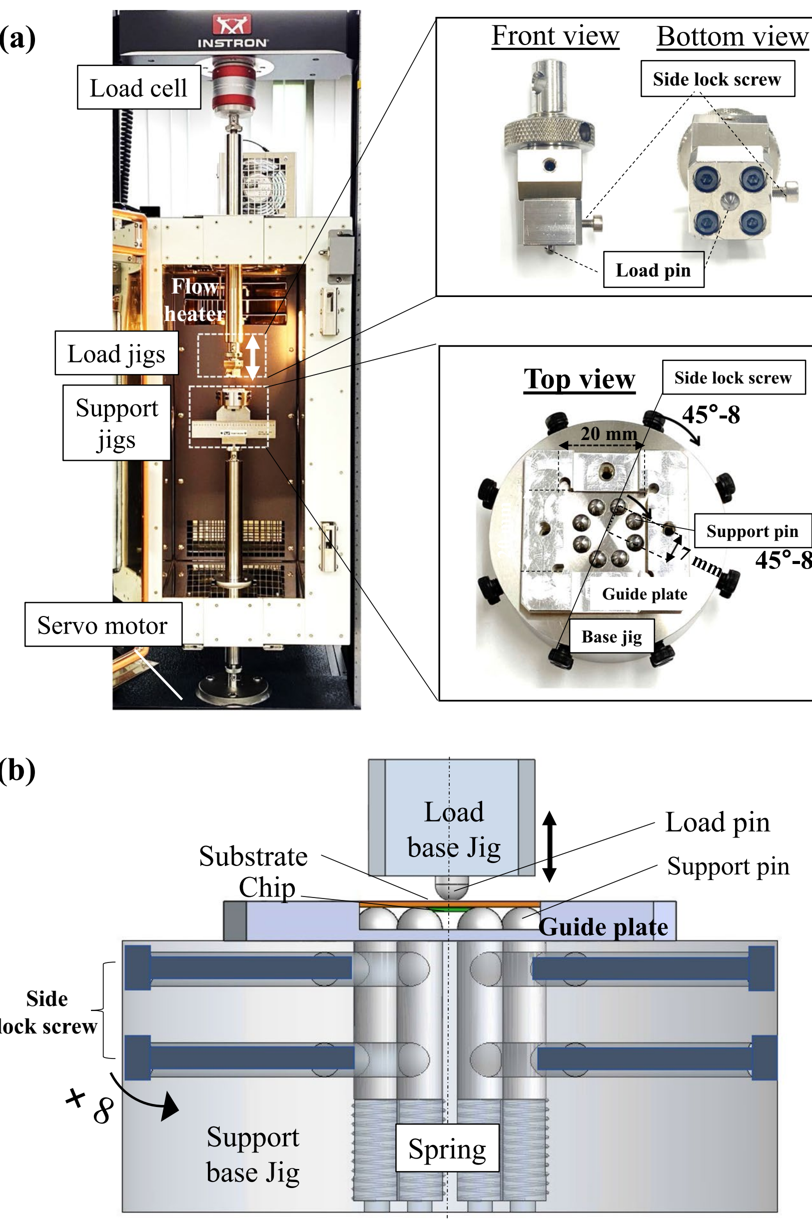

Fig. 2 (**a**) Photographs of NBT experiment system (**b**) Cross-section sketch view of NBT

Experiment Conditions

Table 2 summarizes the test conditions used in this work. In TST, the commercial chamber (Espec Japan: TSA41-EL-A, Osaka, Japan) has a test temperature profile of – 40℃ to 150℃. The travel time between the lowest and highest temperature was set at 25 s. The period time per cycle was set at 60 min, which indicates that the ramp time with each temperature was set at 30 min in the temperature profile. The DAA in TST comprises SiC device, s–Ag bonding layer, and Cu substrate with an electroplate-silver layer, which has been used in power module products owing to its high heat conductivity. With respect to DAA fabrication, the nano-Ag paste possessing silver particles having a diameter of 20 mm was screen-printed on a Cu substrate surface with a 7-mm square hole with a stencil mask. The printed layer thickness was controlled at 200 µm. The printed Ag layer was dried at 140℃ for 90 min and then sintered under 60 MPa pressure at 300℃ for 10 min via a 0.5 mm thick carbon sheet (TOYOTANSO: VVF30, Osaka, Japan) in the air. The porosity was found to be 5%, which was low enough for obtaining a stabilized mechanical property as adopted in my previous research condition [18]. The final bonding thickness was controlled at 50 µm.

The force amplitude in NBT is controlled from 0 to 300N under triangle waveform with 3 min period time. The time taken to travel from 0 to 300N was 90 s.

Table 2 Test conditions

TST	
Amplitude	-40 to 150°C
Period	60 min
Wave form	Rectangular
Assembly	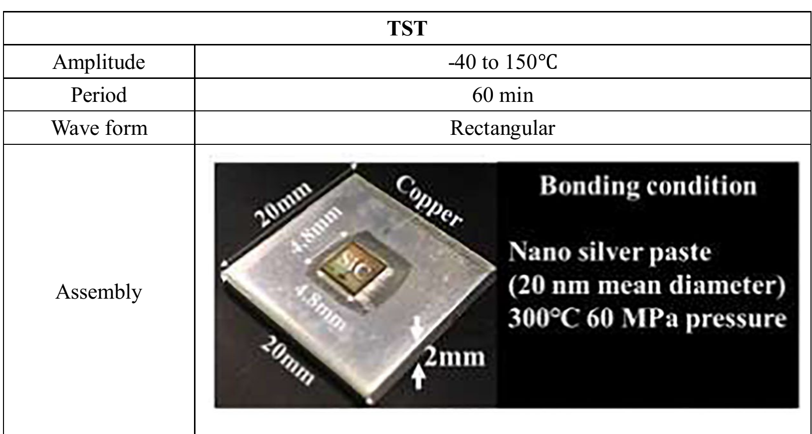

NBT (150°C)	
Amplitude	0-300N
Period	3min
Wave form	Triangle
Assembly	20mm, 64Ti, 4.8 mm, 4.8 mm, SiC, 20mm, 1mm; Bonding condition: Nano silver paste (20 nm mean diameter) 300°C 60 MPa pressure

Moreover, the DAAs fabrication methodology was identical to those with DAAs in TST, except for the substrate material. 64Ti with Ag sputtered substrate was adopted in NBT. The 64Ti mechanical property of Young's modulus is identical to that of the Cu material; however, the yield stress was about three times higher than that of Cu [29]. Therefore, 64Ti substrate can allow bending deformation without fatigue plastic deformation during the NBT. The test temperature was kept constant at 150℃ by heat flow, which was regulated by the feedback signal of the resistance thermometer installed in the chamber. NBT was performed after 60 min to stabilize the temperature in this experiment.

Results and Discussion

Die Delamination Evaluation

Figure 3(a) shows the SAT images after TST and NBT that were obtained by an ultrasonic probe at 25 MHz. The color difference is attributed to the reflective acoustic intensity. The white color depicts the delaminated area having high reflective intensity caused by the presence of air, whereas the black color represents the bonded area without pores. The delamination pattern was roughly categorized into two groups after TST. For TST-1, the delamination portion initially emerged at the corner of the edge after 400 cycles and progressed inside up to 1000 cycles, where similar delamination speeds were observed at each corner [24, 30, 31]. The experimental results coincided with the APS distribution in the s–Ag die layer, which was concentrated at the corner part (Fig. 1(c)). The TST-2 delamination also started from the corners after 400 cycles, but the delamination randomly proceeded after 800 to 1000 cycles, indicating that another fracture mode was composited from 800 to 1000 cycles.

For NBT, the delamination occurred at the upper corners after 400 cycles. Subsequently, large delamination occurred from the left side to the inside from 600 to 1000 cycles. This experiment result also coincided with the s–Ag die layer concentrated at the corner part (Fig. 1(c)).

Figure 3(b) presents the delamination ratio as a function of the number of cycles. In the figure, the red and black plots indicate the results for TST and NBT, respectively. The delamination ratio refers to the ratio of the white-colored area in a SAT image to the entire SiC

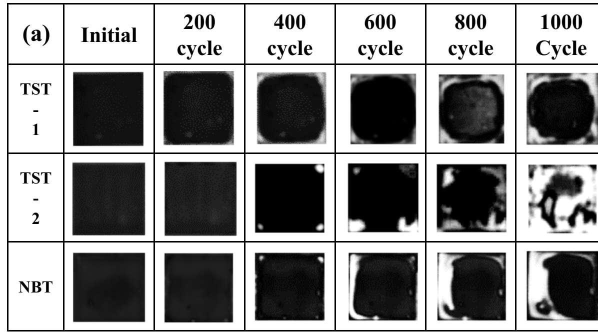

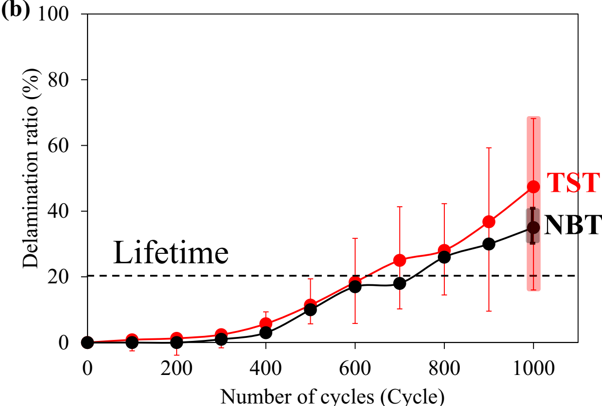

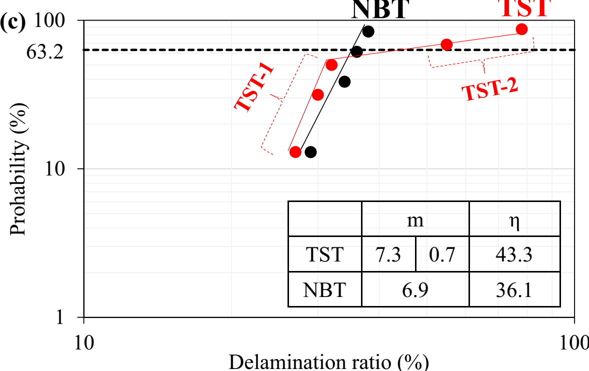

	m		η
TST	7.3	0.7	43.3
NBT	6.9		36.1

Fig. 3 (**a**) Representative scanning acoustic tomography images after TST and NBT (**b**) Delamination ratio as a function of the number of cycles (**c**) Weibull plot of the delamination ratio after 1000 cycles in TST and NBT

device size. Lifetime is defined as 20% delamination ratio, as stated in the Introduction section [22, 24–27]. For each test, five specimens were evaluated. Dispersion evaluation in TST was undertaken every 100 cycles, while that for NBT was undertaken after 1000 cycles. Both TST and NBT showed similar mean values of the delamination ratio at the respective cycles. The samples for each test reached the lifetime defined at approximately 600 cycles. This result indicates that mechanical stress plays a significant role in deteriorating the s–Ag die bonding layer up to the lifetime cycles in both tests. In other words, the lifetime evaluation using TST and using NBT are similar and can be used interchangeably. Furthermore, NBT reduces the reliability evaluation period by 1/20 compared to TST. However, the dispersion of the delamination ratio in TST increased from approximately 500 cycles to 1000 cycles. A comparison of the dispersion values of the delamination ratios shows that the error bar length of the delamination ratio value in TST was approximately five times higher than that in NBT at 1000 cycles.

Figure 3(c) shows the Weibull plot of the delamination ratio after 1000 cycles in TST and NBT. The definition of plot color is identical to that in Fig. 3(b). Here, the probability is derived using the median rank methodology [22]. The m value defines the line slope value in the Weibull static sheet, which is associated with the deviation of the delamination ratio among evaluated samples. A small m value indicates that the delamination ratio value is scattered from sample to sample. The η value is defined as a 63.2% probability value in delamination ratio after 1000 cycles derived from Weibull plots. In NBT, the plot can be fitted with only one approximation line, indicating that a single two-parameter of m and η can fit the data in NBTs. This finding indicates that all evaluated samples are fractured under a sole failure mechanism in NBT that is associated with mechanical stress. The m and η values in NBT were found to be 6.9 and 36.1, respectively. On the other hand, the Weibull distribution for TST showed data scattering that can be approximated using two straight lines. This finding indicates that a series of evaluated samples failed under multiple fracture modes. The representative degradation appearance of the first and second slope groups corresponded to the SAT images of TST-1 and TST-2, respectively. The m value on the low-delamination side of TST-1 was 7.3, which is comparable to that of NBT. However, its value on the high-delamination side of TST-2 was 0.7, which is a meager value compared to that of TST-1 and NBT. The TST-2 group delamination is scattered from sample to sample, which means destabilized failure mode. The delamination among TST-2 groups would be affected by multiple failure causes, indicating both mechanical stress and thermal effect. The η value of TST was 43.3%, which was similar to that of NBT.

Failure Mode

Cross-sectional SEM observations were performed after 1000 cycles to understand the difference in fracture mode between TST-2 and NBT. Figure 4 shows that the cross-section of the s–Ag die layer for NBT included only cracks. A crack generally propagated from the SiC corner into the s–Ag die layer

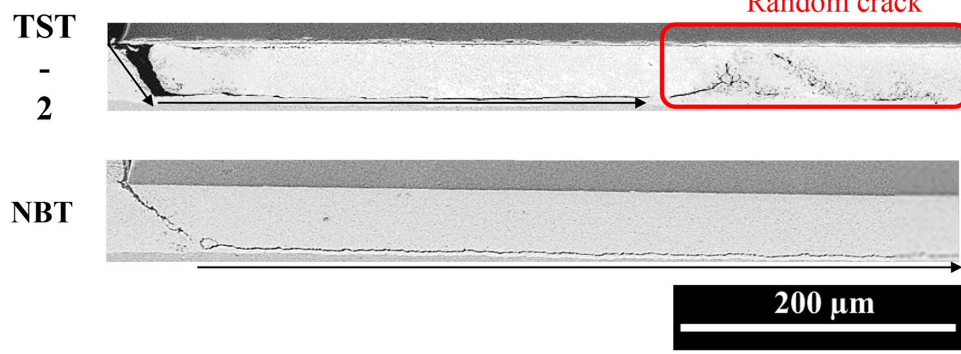

Fig. 4 Representative cross-sectional SEM observation results after 1000 cycles of TST and NBT

at approximately 45° to the substrate. The direction of the crack changed to the horizontal direction at the s–Ag die layer and substrate interface. For TST and NBT, a crack was introduced at the SiC corner, which then propagated to the inside at approximately 45°. The crack path changed to the direction along the substrate surface but became discontinuous at the middle section. In this region, pore growth led to stress concentration working as a new crack generation region, which destabilized the s–Ag die fracture as shown in the previous literature [27]. This fracture mode was primarily due to the thermal material aging effect, as determined through the comparison of failure mode between TST and NBT in this study. The s–Ag material aging phenomenon can be explained by Ostwald's ripening law, which is a classical thermally driven microstructure evolution [15]. According to this law, microstructure aging becomes active with the increase in high temperature holding time. Accordingly, mechanical force variation with triangle waveform with short period time of 3 min would not cause s–Ag material aging in the case for NBT. However, TST controlled with rectangular thermal waveform of long holding time of 30 min would result in s–Ag material aging. Note that the s–Ag material aging will change completely APS distribution in the s–Ag die layer with increasing the stress concentration area surrounding the pore growth area as depicted in the previous literature's simulation results [27]. This fact indicates that the simulation results of APS distribution in the s–Ag die layer (Fig. 1(c)) could not be reflected during failure evaluation in TST with s–Ag material aging. Ideally, the assembled elements of the power module does not deteriorate thermally in the bonded layer. The TST evaluation is replaceable by the NBT as an acceleration reliability testing method if the main fracture failure mode up to the lifetime is regarded as cracking caused only by mechanical stress. The validity of the correlation between the TST and NBT results should be examined by different types of DAAs and cycling patterns to identify the contribution of material aging and mechanical stress to the s–Ag die failure. The material aging mechanism, including the microstructure state of the crystal pore, should also be considered to determine a strategy for improving the s–Ag die lifetime.

Conclusions

In this study, the main causes of s–Ag degradation during TST were determined by using a new mechanical bending test called NBT. SAT images after TST and NBT revealed that the mean delamination ratio in TST overlapped with that in NBT up to 1000 cycles. This result indicated that mechanical stress was played the main role in deteriorating the s–Ag die layer during TST. On the other hand, the dispersion value of delamination ratio after 1000 cycles in TST was five times higher than that in NBT after 1000 cycles. Weibull plot of delamination ratio after 1000 cycles with TST showed data scattering, which fitted into two different approximation lines. In this case, at least two delamination mechanisms coexisted in the TST. In comparison, NBT showed only one linear line fitting. The SEM images after 1000 cycles revealed that TST had two cracking modes with straight cracking and zigzag cracking that originated from thermal aging. On the contrary, NBT failure mode had only straight cracking. This finding indicated that TST simultaneously deteriorated thermally with increasing number of cycles. In our future study, we will check the validity of the correlation between the TST and NBT results by using different types of DAAs and cycling patterns so as to examine the contribution of material aging and mechanical stress to s–Ag die layer failure.

Data Availability The datasets generated and/or analyzed during the current study are available from the corresponding author on reasonable request.

Declarations

Conflicts of Interests/Competing Interests The authors declare no conflicts of interests/competing interests.

Open Access This article is licensed under a Creative Commons Attribution 4.0 International License, which permits use, sharing, adaptation, distribution and reproduction in any medium or format, as long as you give appropriate credit to the original author(s) and the source,

provide a link to the Creative Commons licence, and indicate if changes were made. The images or other third party material in this article are included in the article's Creative Commons licence, unless indicated otherwise in a credit line to the material. If material is not included in the article's Creative Commons licence and your intended use is not permitted by statutory regulation or exceeds the permitted use, you will need to obtain permission directly from the copyright holder. To view a copy of this licence, visit http://creativecommons.org/licenses/by/4.0/.

References

1. She X, Huang AQ, Lucia O, Ozpineci B (2017) Review of silicon carbide power devices and their applications. IEEE Trans Industr Electron 64:8193–8205. https://doi.org/10.1109/tie.2017.2652401
2. Hudgins JL, Simin GS, Santi E, Khan MA (2003) An assessment of wide bandgap semiconductors for power devices. IEEE Trans Power Electron 18:907–914. https://doi.org/10.1109/tpel.2003.810840
3. Biela J, Schweizer M, Waffler S, Kolar JW (2011) SiC versus Si—evaluation of potentials for performance improvement of inverter and DC–DC converter systems by SiC power semiconductors. IEEE Trans Ind Electron 58:2872–2882. https://doi.org/10.1109/tie.2010.2072896
4. Neudeck PG, Okojie RO, Chen L-Y (2002) High-temperature electronics—a role for wie bandgap semiconductors? Proc IEEE 90:1065–1076. https://doi.org/10.1109/JPROC.2002.1021571
5. Siow KS (2014) Are sintered silver joints ready for use as interconnect material in microelectronic packaging? J Elec Mat 43:947–961. https://doi.org/10.1007/s11664-013-2967-3
6. Siow KS (2012) Mechanical properties of nano-silver joints as die attach materials. J Alloy Compd 514:6–19. https://doi.org/10.1016/j.jallcom.2011.10.092
7. Peng P, Hu A, Gerlich AP, Zou G, Liu L, Zhou YN (2015) Joining of silver nanomaterials at low temperatures: processes, properties, and applications. Appl Mater Interfaces 7:12597–12618. https://doi.org/10.1021/acsami.5b02134
8. Bai JG, Calata JN, Lu GQ (2007) Processing and characterization of nanosilver pastes for die-attaching sic devices. IEEE Trans Elecronics Packag Technol 30:241–245. https://doi.org/10.1109/TEPM.2007.906508
9. Wereszczak AA, Vuono DJ, Wang H, Ferber MK, Liang ZH (2012) Properties of Bulk Sintered Silver As a Function of Porosity. Oak Ridge, Report No. ORNL/TM-2012/130
10. Ordonez-Miranda J, Hermans M, Nikitin I, Kouznetsova VG, van der Sluis O, Ras MA, Reparaz JS, Wagner MR, Sledzinska M, Gomis-Bresco J, Sotomayor Torres CM, Wunderle B, Bolz S (2016) Measurement and modeling of the effective thermal conductivity of sintered silver pastes. Int J Therm Sci 108:185–194. https://doi.org/10.1016/j.ijthermalsci.2016.05.014
11. Bai JG, Chang ZZ, Calata JN, Lu GQ (2006) Low-temperature sintered nanoscale silver as a novel semiconductor device-metallized substrate interconnect material. IEEE Trans Device Mater Reliab 29:589–593. https://doi.org/10.1109/TCAPT.2005.853167
12. Chen CJ, Chen CM, Horng RH, Wu DS, Hong JS (2010) Thermal management and interfacial properties in high-power GaN-based light-emitting diodes employing diamond-added Sn-3 wt.%Ag-0.5 wt.%Cu solder as a die-attach material. J Electron Mater 39:2618–2626. https://doi.org/10.1007/s11664-010-1354-6
13. Thomas M (2007) A lead-free solution for power and high-power applications. Adv Packag 39:32–34
14. Zabihzadeh S, Petegem SV, Duarte L, Mokso R, Cervellino A, Swygenhoven HV (2015) Deformation behavior of sintered nanocrystalline silver layers. Acta Mater 97:116–123. https://doi.org/10.1016/j.actamat.2015.06.040
15. Gadaud P, Caccuri V, Bertheau D, Carr J, Milhet X (2016) Ageing sintered silver: relationship between tensile behavior, mechanical properties and the nanoporous structure evolution. Mater Sci Eng A 669:379–386. https://doi.org/10.1016/j.msea.2016.05.108
16. Suzuki T, Terasaki T, Kawana Y, Ishikawa D, Nishimura M, Nakako H, Kurafuchi K (2016) Effect of manufacturing process on micro-deformation behavior of sintered-silver die-attach material. IEEE Trans Device Mater Reliab 16:588–596. https://doi.org/10.1109/TDMR.2016.2614510
17. Wakamoto K, Mochizuki Y, Otsuka T, Nakahara K, Namazu T (2020) Temperature dependence on tensile mechanical properties of sintered silver film. Materials 13:4061. https://doi.org/10.3390/ma13184061
18 Wakamoto K, Mochizuki Y, Otsuka T, Nakahara K, Namazu T (2019) Tensile mechanical properties of sintered porous silver films and their dependence on porosity. Jpn J Appl Phys 58:SDDL08. https://doi.org/10.7567/1347-4065/ab0491
19. Webber C, Dijk MV, Walter H, Hutter M, Witter O, Lang KD (2016) Combination of Experimental and Simulation Methods for Analysis of Sintered Ag Joints for High Temperature Applications. Proc 66rd Electron Compon Technol Conf (ECTC):1335–1341. https://doi.org/10.1109/ECTC.2016.394
20. Suganuma K, Kim SJ, Kim KS (2009) High-temperature lead-free solders: properties and possibilities. JOM 61:64–71. https://doi.org/10.1007/s11837-009-0013-y
21. Herboth T, Guenther M, Zeiser R, Wilde J (2013) Investigation of Stress States in Silicon Dies Induced by the Low Temperature Joining Technology 14th Int Con on Thermal, Mechanical and Multi-Physics Simulation and Experiments in Microelectronics and Microsystems (EuroSimE):1–6. https://doi.org/10.1109/EuroSimE.2013.6529945
22. Herboth T, Guenther M, Zeiser R, Wilde J (2012) Assessment of thermo-mechanical stresses in Low Temperature Joining Technology. 13th Int Con on Thermal, Mechanical and Multi-Physics Simulation and Experiments in Microelectronics and Microsystems (EuroSimE):1–7. https://doi.org/10.1109/ESimE.2012.6191762
23. Rajaguru P, Lu H, Bailey C (2015) Sintered silver finite element modelling and reliability based design optimisation in power electronic module. Microelectron Reliab 55:919–930. https://doi.org/10.1016/j.microrel.2015.03.011
24. Wakamoto K, Matumoto R, Namazu T (2022) SiC Power Module Design: Performance, Robustness (The Institution of Engineering and Technology) Chapter 10. https://doi.org/10.1049/PBPO151E_ch10
25. Herboth T, Guenther M, Fix A, Wilde J (2013) Failure mechanisms of sintered silver interconnections for power electronic applications. Proc 63rd Electron Compon Technol Conf (ECTC):1621–1627. https://doi.org/10.1109/ECTC.2013.6575789
26. Schaal M, Klingler M, Matais B, Grueninger R, Hoffmann S, Wunderle B (2020) Reliability Assessment of Ag Sintered Joints Using a SiC Semiconductor and Determination of Failure Mechanism in the Field of Power Electronics. 20th Int Con on Thermal, Mechanical and Multi-Physics Simulation and Experiments in Microelectronics and Microsystems (EuroSimE): 1–12. https://doi.org/10.1109/EuroSimE48426.2020.9152674
27. Wakamoto K, Otsuka T, Nakahara K, Namazu T (2021) Degradation mechanism of pressure-assisted sintered silver by thermal shock test. Energies 14:5532. https://doi.org/10.3390/en14175532
28. Heilmann J, Nikitin I, Zschenderlin U, May D, Pressel K, Wunderle B (2017) Reliability experiments of sintered silver based interconnections by accelerated isothermal bending tests.

Microelectron Reliab 74:136–146. https://doi.org/10.1016/j.microrel.2017.04.016

29. Wang C, Shang C, Xu G, Jing Z, Liu J, Su Y (2020) Microstructure and mechanical property improvement of laser additive manufacturing Ti-6Al-4V via the niobium addition. Mater Trans 61(4):723–728. https://doi.org/10.2320/matertrans.MT-M2019370
30. Mroszko R, Opperman H, Wunderle B, Michel B (2011) Reliability analysis of low temperature low pressure Ag-sinter die attach. NSTI Nanotechnology conference and Expo:149–154
31. Wakamoto K, Mochizuki Y, Otsuka T, Nakahara K, Namazu T (2022) Comparison of sintered silver die attach failure between thermal shock test and mechanical cycling test. Jpn J Appl Phys 61:SD1029. https://doi.org/10.35848/1347-4065/ac5b23

Publisher's Note Springer Nature remains neutral with regard to jurisdictional claims in published maps and institutional affiliations.